Contractile response of alveolar epithelial cells to biochemical or mechanical stimulation probed by traction microscopy

Núria Gavara i Casas

Contractile response of alveolar epithelial cells to biochemical or mechanical stimulation probed by traction microscopy

A dissertation by
Núria Gavara i Casas
in partial fulfilment of the requirements for
the degree of Doctor of Philosophy

Thesis supervisor : Prof. Ramon Farré i Ventura

Unitat de Biofísica i Bioenginyeria
Dept. de Ciències Fisiològiques I
Facultat de Medicina, Universitat de Barcelona.

Chapter 3. Traction microscopy to probe contractile forces of alveolar epithelial cells

3.1 Introduction

This chapter is divided into three sections. The first section describes the algorithms proposed by Tolic-Norrelykke (Tolic-Norrelykke et al., 2002) and Butler (Butler et al., 2002) to compute gel deformation and the corresponding traction field. In addition, some parameters reflecting cell contractility are presented. The second section of this chapter describes the gel substrates used. The most suitable gel substrate and optimal stiffness was adjusted. Moreover, the main characteristics of the acquired fluorescence images of the gels and the imaging device employed are described. Finally, the third chapter's section presents the results of the simulations performed to check the software which was written to perform the TM algorithms described in the first section. These simulations enabled the determination of the optimal value for some experimental parameters, such us the number of beads used or the displacement of the beads. The results obtained in the simulations show that our measurements were performed under suitable experimental conditions, providing information on the precision of our traction microscopy results.

3.2 Traction microscopy algorithms

3.2.1 Computation of the displacement field

An essential step in obtaining reliable traction values is to accurately estimate the displacement fields from images of the fluorescent microbeads in the gel. We used the method known as Image Correlation Method (ICM) described by Tolic-Norrelykke and coworkers (Tolic-Norrelykke et al., 2002). This method is based on using the cross-correlation function of two windows to iteratively find the displacement field between images of the cell-stressed gel and the cell-free reference image. The cross-correlation function is the similarity measure between a window from image A and windows in image B located at various space lags. The coordinates of the peak of the correlation function correspond to the displacement between the window in image A and the most similar window found in image B (Fig. 3.1).

To enable fast computations, calculi of the cross-correlation are performed in the Fourier space:

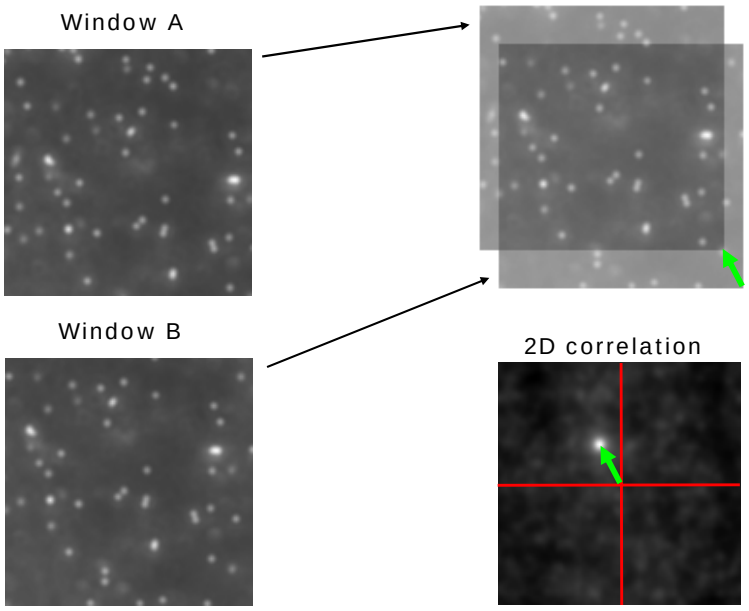

Fig. 3.1 2D correlation to compute the translational shift between a pair of windows. Window A and B display a similar patter but exhibit a relative translational shift (green arrow). To compute this vectorial shift, 2D correlation of the two windows is performed. The vector linking the origin of coordinates and the peak of the correlation corresponds to the translational shift between the two windows.

$$Corr(A,H) = \frac{Corr'(G,H)}{\sqrt{\max\left[Corr'(G,G)\right]\max\left[Corr'(H,H)\right]}} \qquad FT_2\left[Corr'(G,H)\right] = FT_2(G)\,FT_2(H)^*$$

where FT_2 denotes the two dimensional Fourier transform, *Corr* is the correlation of two functions, A and B are two functions (two images in this case), and the asterisk denotes complex conjugation. To obtain subpixel displacement values, the peak of the cross-correlation function is found by fitting the values of the function in the immediate neighbourhood of the pixel with the highest value to a second order polynomial (Tolic-Norrelykke et al., 2002).

The computation algorithm proceeds as follows (Fig. 3.2) (Tolic-Norrelykke et al., 2002).The first step in the displacement field computation is the correction for whole image relative translational shift. The cross-correlation of the two images is computed as described above and image B is subsequently translated with respect to image A by the resulting displacement vector as a uniform displacement. Next, the displacement field between the two corrected images is calculated starting from a low spatial resolution and refining the calculation to higher and higher resolution. Images are first divided into large distinct windows and the displacement of each window is calculated. Image B is then

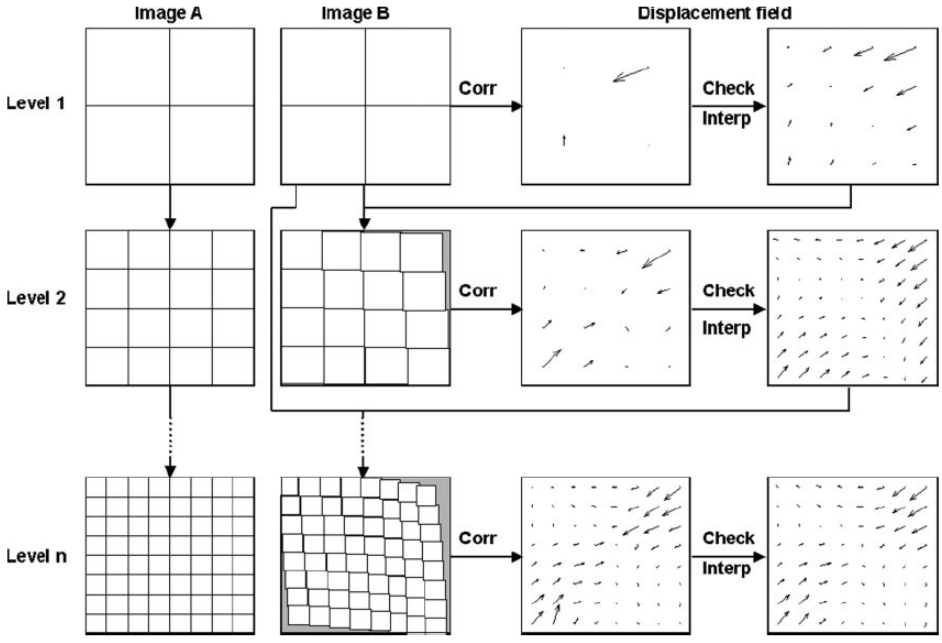

Fig. 3.2 Iterative algorithm to compute the displacement field between a pair of images. Adapted from (Tolic-Norrelykke et al., 2002).

distorted by this displacement field and the procedure is repeated for all the windows. At each succeeding level of the iteration, the spatial resolution of the displacement vectors is twice that of the previous level. Furthermore, at each new iteration level, only the residual displacements are computed and added to the initial ones, giving a refined result. The whole procedure is repeated until the selected spatial resolution is obtained. An example of fields displaying the magnitude of displacement obtained for different final spatial resolutions is shown in Fig. 3.3

To reduce errors in the displacement field, some checkpoints are included at each level (Tolic-Norrelykke et al., 2002). A pair of windows has to pass all these tests; otherwise, the displacement of that window is temporally set to an undefined value. The tests are used to assert that the windows contain some fluorescent beads but do not contain bead clusters. It should be noted that at each level only small corrective displacements are expected. Therefore, another test is set up to make sure that the computed corrective displacement of the window is not erroneously too large. In our implemented software, this is done by establishing a check parameter (max) which constitutes a fractional value of the window size at each iteration. Therefore, the implemented algorithm permits only corrective displacements smaller than this fraction (window size/max). Proper adjustment of the max parameter allows the reduction of noise without underestimating the real observed displacement. Finally, displacement values for the windows that did not pass some of the checkpoints (and were temporally set to an undefined value) are computed later by

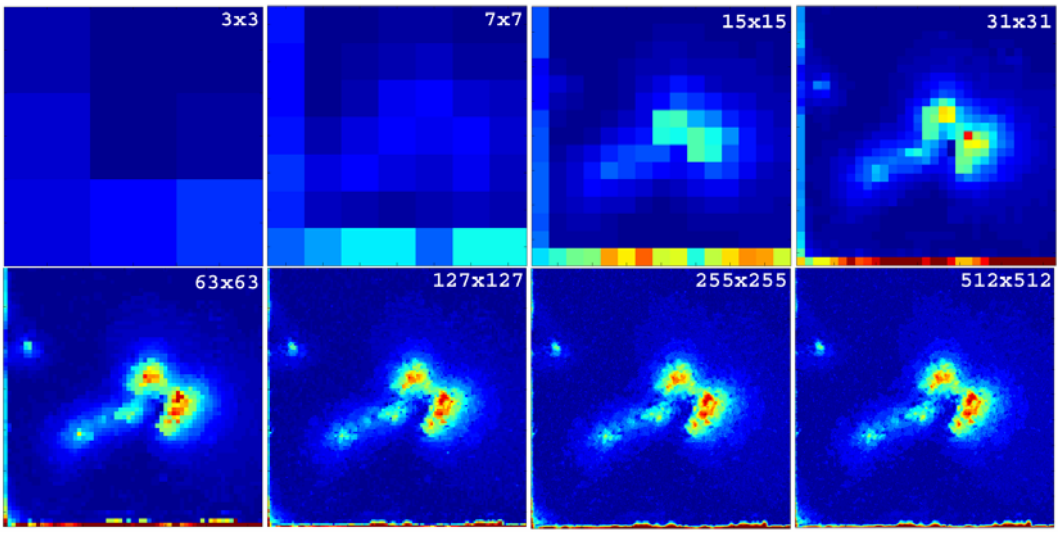

Fig. 3.3 Example of the iteration process performed to obtain a displacement field exerted by an A549 cell. At each iteration the spatial resolution of the field is doubled until the established resolution is reached.

interpolating the displacement values from neighbouring windows.

The software written to perform this algorithm is displayed in Appendix D. The software was programmed using LabVIEW (National Instruments, Austin, TX).

3.2.2 Computation of the traction field

The deformation of an elastic substratum is related to the applied traction field via an integral transform:

$$d_\alpha = \iint g_{\beta\alpha}\left(\bar{m}-\bar{r}\right)T_\beta(\bar{r})dr_1dr_2$$

where the Greek subscripts take on values 1, 2, and 3 and summation over repeated indices is implied. The nine functions $g_{\beta\alpha}(\bar{m}-\bar{r})$ (coefficients of a Green's tensor) can be derived from the theory of Boussinesq (Landau and Lifshitz, 1986) and give the displacement of the substratum in the direction α at location m induced by a concentrated force in the direction β acting at location r. It turns out that at or near the surface of an incompressible substratum the Boussinesq theory predicts negligible coupling of in-plane displacements to out-of-plane tractions, (i.e., g_{13}=g_{23}=0). As a result, the tangent projection of marker displacement as measured in traction microscopy experiments, (d_1, d_2), is a function of the tangent projection of the traction field (T_1, T_2) only. Therefore, observations of the z component of bead displacement are not needed for successful numerical deconvolution of the traction field (Butler et al., 2002).

Computation of the resulting displacement field from the distribution of surface tractions constitutes the so-called forward problem. The problem addressed in traction microscopy computations is the inverse problem, namely inferring the traction field from measured displacements. We have used the computational approach described by Butler and coworkers (Butler et al., 2002) to obtain the traction field from the measured displacement field. This approach is based on the Fourier analysis and is computationally efficient and exact in the sense that it yields a traction map for which the induced displacements exactly match the given displacement field. The solution to the inverse problem computed in the Fourier space is then given by:

$$\overline{T} = FT_2^{-1}\left(\widetilde{K}^{-1}\widetilde{\overline{u}}\right) \qquad \widetilde{K} = \frac{2(1+\sigma)}{Ek^3}\begin{pmatrix}(1-\sigma)k^2+\sigma k_y^2 & \sigma k_x k_y \\ \sigma k_x k_y & (1-\sigma)k^2+\sigma k_x^2\end{pmatrix}$$

where FT_2^{-1} denotes the two dimensional inverse Fourier transform, σ is Poisson's ratio and E is Young's modulus.

All approaches that compute traction fields from displacement fields explicitly approximate the elastic gel as a semi-infinite medium. Nevertheless, it must be kept in mind that this approximation is valid if the lateral dimensions of the cell and the lateral distances over which displacements are measured are both small compared with the gel thickness (Butler et al., 2002).

Constrained FTTC

Once the displacement field is obtained, computation of cell tractions can be performed in two distinct ways. The first method, unconstrained FTTC, uses all displacement data from an image pair, does not use any constraints on the recovered tractions, and is a direct application of the computation of traction forces described above. The second method, Constrained FTTC, is the solution to the mixed boundary value problem, which ignores the measured displacement field outside the boundary of the cell and constrains the tractions outside the cell boundary to be zero (Butler et al., 2002). It is important to note that this method requires additional information beyond the displacement field, namely an estimate of the location of the cell boundary. We have used Constrained FTTC to compute the traction field because this method enabled discarding tractions generated by proximal cells which would erroneously contribute to the cell contractility parameters. The specific procedure to iteratively compute CFTTC is as follows (Butler et al., 2002):

1. The traction field is calculated directly from the displacement field using the equations described above.
2. A new traction field is defined by setting the tractions outside of the cell boundary to zero.
3. The displacement field induced by this traction field is calculated. This is done by using the Fourier approach in the forward direction: calculating the Fourier transform of the traction field and multiplying by $\widetilde{K}\left(\vec{k}\right)$ to obtain the transformed

displacements. The inverse Fourier transform of the result is then the new displacement field.

4. A new displacement field is defined by replacing the displacements of the calculated displacement field within the cell boundary by the experimentally observed displacements.
5. Steps 1–4 are repeated until convergence is reached at some level of tolerance. We chose to terminate the iterative procedure when the variation in the maximum magnitude of the tractions within the cell was less than 1 part in 10^6 on succeeding steps.

The software written to perform this algorithm is displayed in Appendix D. The software was programmed using LabVIEW (National Instruments, Austin, TX).

3.2.3 Parameters that reflect cell contractility

The previously described algorithms provide the traction field exerted by an adhered cell. To obtain a single estimate of the cell contractility or contractile state, several parameters have been proposed by different authors.

Total Force Magnitude (F) and Average Traction Magnitude (T)

An overall measure of cellular contractility is obtained by computing the total force magnitude, defined as:

$$F = \iint \left| \overline{T} \right| dxdy$$

Dividing F by the cell area A yields the average traction magnitude, which is a measure of the average absolute force per unit area exerted within the cell (Gaudet et al., 2003).

Net contractile moment (M)

The net contractile moment is computed as:

$$M = M_{xx} + M_{yy} \qquad \text{where} \qquad M_{ij} = \frac{1}{2} \iint \left[x_i T_j \left(\bar{r} \right) + x_j T_i \left(\bar{r} \right) \right] dxdy$$

The total contribution of the cell to contracting the substrate in the x and y

directions (radially oriented tractions) is given by M_{xx} and M_{yy}, respectively. M_{xy} or M_{yx} are the contributions of the cell to a deformation of the substrate arising from variations in x tractions with y and variations in y tractions with x (tractions corresponding to torques). As a visual aid, the four terms are shown schematically in the diagrammatic representation above. The net contractile moment tending to dilate or contract the substrate is given by the trace of the moment matrix (Butler et al., 2002).

$$\begin{bmatrix} xT_x & xT_y \\ yT_x & yT_y \end{bmatrix} \leftrightarrow$$

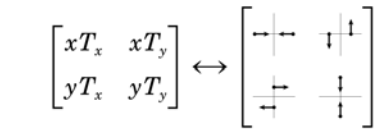

The contractile moment can be thought of an equivalent force generator comprising only two imaginary point forces (F) that are equal, opposite, and separated by a distance (d) (Butler et al., 2002). This equivalent force generator "pinches" the elastic substrate to the same extent as does the cell. The contractile moment (M) is simply the product $F \cdot d$. Interestingly, if the geometry of the adherent cell does not change appreciably during the contractile event, it follows on dimensional grounds that the prestress must be proportional to the contractile moment (Wang et al., 2002).

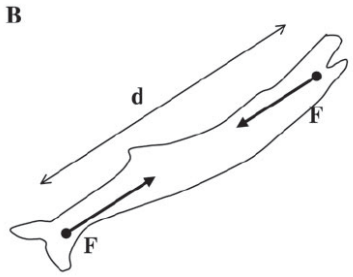

The components of the moment matrix also provide an index of the polarity of cell contraction. This is computed as the ratio of the contractile moment along the principal axis of traction M_{xx} to the net contractile moment M, and is thus restricted between 0.5 and 1 (Tolic-Norrelykke et al., 2002).

Strain energy (U)

The strain energy is the total energy transferred from the cell to the elastic distortion of the substrate. It is computed as follows:

$$U = \frac{1}{2}\iint \bar{T}\left(\bar{r}\right)\bar{d}\left(\bar{r}\right)dxdy$$

The net contractile moment is given in units of picoNewton times meters (pN·m) and energy is given in units of picoJoules (pJ). These units are used to distinguish clearly between moments (forces multiplied by distances from the origin) and energy (forces multiplied by displacements), despite the fact that pN·m and pJ are formally equivalent (Butler et al., 2002).

3.3 Implemented traction microscopy setups to probe contraction of alveolar epithelial cells

3.3.1 Selected gel substrates and optimization of gel stiffness

The magnitude of bead displacement depends on both the stiffness of the substrate and the magnitude of traction forces exerted by the adhered cell. Therefore, for each cell type, care must be taken to produce elastic gels with an optimal Young's Modulus, resulting in measurable bead displacements. Too stiff gels will result in unresolvable bead displacements, whereas too soft gels will induce excessively large displacements that will be erroneously measured. The standard gel substrate for traction microscopy experiments is polyacrilamide (Dembo and Wang, 1999;Butler et al., 2002;Curtze et al., 2004;Stamenovic et al., 2002). The main benefit of polyacrylamide is that its stiffness can be readily adjusted by controlled variations of the monomer and cross-linker concentrations. To provide a physiological surface for cell culture, a saturating density of type I collagen is covalently attached to the exposed surface of the polyacrylamide gel. Furthermore, 3D traction microscopy has been recently implemented (Mierke et al., 2006). Since the cells must be embedded into the elastic gel, collagen gels constitute the standard gel matrix for this kind of studies.

In our traction microscopy experiments two different gel substrates were used. To study the effect of thrombin in alveolar epithelial cells (see 0), polyacrylamide gels were employed. Previous to the development of the experiments, the stiffness of the polyacrylamide gels, and thus the concentration of acrylamide monomer and crosslinker had to be adjusted for our studied cell type. Once the selected concentration of monomer

and crosslinker was observed to provide optimal bead displacements for alveolar epithelial cells, the Young's Modulus of the resulting gels was measured by atomic force microscopy (AFM). The detailed protocol used to produce collagen I coated polyacrylamide gels can be found in Appendix A. Young's Modulus of the polyacrylamide gels are reported on Chapter 40. To study the effect of stretch in alveolar epithelial cells, elastic gels had to polymerize onto silastic membranes and stay firmly attached during membrane distention. Since polyacrylamide gels did not fulfil these requirements, collagen gels were used. In this case, the concentration of collagen was optimized to provide fiberless homogeneous gels that polymerized and attached to the silastic membrane. Again, the Young's Modulus of the resulting gels for each applied strain was measured by AFM once the optimal collagen concentration was established. The protocol used to produce collagen I gels can be found in Appendix B. Young's Modulus of the resulting gels is reported on Chapter 5.

3.3.2 Fluorescence images of the polyacrylamide and collagen gels

Fluorescence images of the gel disks were obtained with a 12-bit-resolution cooled-charge-coupled device camera (Orca, Hamamatsu Photonics) mounted on the stage of an inverted fluorescence microscope (Eclipse TE2000, Nikon). In the study of the effects of thrombin in cell contractility (Chapter 4), the apparent pixel size after magnification (40×) was 0.16 μm with a resulting field of view of $161\times161\mu m^2$. The depth of focus of the used objective was 1.5μm. Imaged fields of the polyacrylamide gels contained ~5000 focused beads, which occupied ~9 pixels/bead. For stretch-induced contraction studies (Chapter 5), the apparent pixel size after magnification (20×) was 0.32 μm with a resulting field of view of $323\times323\mu m^2$. The depth of focus of the used objective was 2.7 μm. Imaged fields of the collagen gels contained ~11000 focused beads, which occupied ~4 pixels/bead. For both types of experiments, image acquisition time was set to 0.3 sec, yielding similar pixel intensities. Average pixel intensity for the fluorescent beads was ~1800 ± 500 counts and intensity of background noise ~900 ± 25 counts.

3.4 Validation of the implemented software

3.4.1 Computation of the displacement field

Generation of deformed bead images

To test the accuracy of the software to compute the displacement field, we simulated bead-containing undeformed and deformed images. First, an undeformed image was constructed with the following characteristics:

1. The beads where randomly distributed over the imaged field.
2. Each image contained 5000 beads.
3. Each bead occupied 9 pixels. The intensity value of the beads followed a Gaussian distribution with mean = 1800 and SD = 500, resembling imaged beads in real experiments. All nine pixels belonging to the same bead had the same intensity.
4. The values of pixels corresponding to background were random numbers following a Gaussian distribution with mean = 900 and SD = 25, resembling background noise.

Fig. 3.4 shows two examples, one corresponding to a real image obtained from a traction microscopy experiment of thrombin-induced cell contraction, and the other one simulated following the characteristics described above.

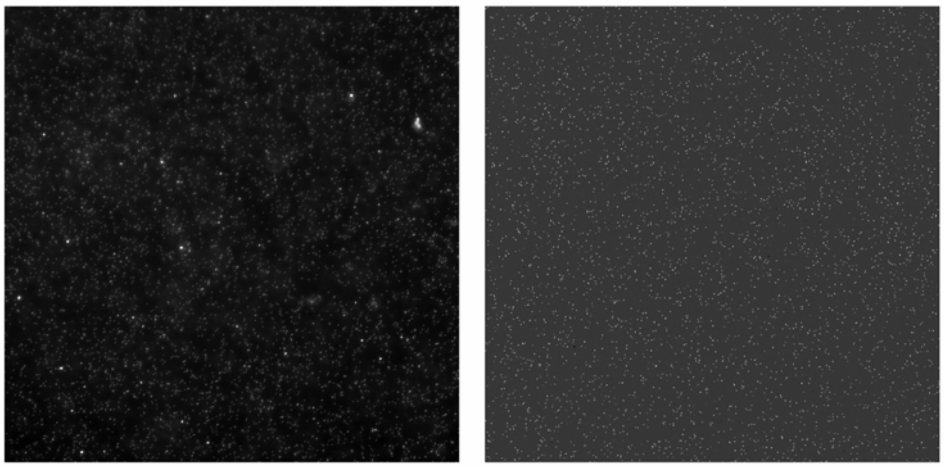

Fig. 3.4 Comparison between a real fluorescence image of the gel used for the study of thrombin-induced contraction (left) and a simulated imaged (right) following the characteristics described above.

Once the undeformed image was generated, a deformed image was constructed by displacing each bead from the undeformed image by *d(x)* pixels in *x* direction and 0 in *y* direction. The displacement function *d(x)* was chosen to be the integer values of two 2D Gaussian peaks, one with positive displacements and the other with negative displacements but both with the same peak amplitude, thus resembling the displacement pattern that a force dipole would induce. An example is shown in Fig. 3.5. After constructing a pair of images in such a way, the images were used as the input to the software to compute the displacement field. The displacement field was calculated and compared with the values of the theoric *d(x)*. An average noise value was computed by pooling all the values $\left|d_{theo}(x,y)-d_{obs}(x,y)\right|$ corresponding to pixels of the displacement field with $d_{theo}(x,y)\neq 0$. For each simulation, the SNR value was computed by dividing the amplitude of the peak by the average noise.

Effect of fluorescence images and gel displacement characteristics on the SNR of the displacement field

Simulations were performed to assess the effect of the number of imaged beads and the fluorescence background noise in the SNR of the obtained displacement field. Moreover, different peak amplitudes and max values were used to study the limits of applicability of our software and the optimal max values to reduce noise while avoiding displacement underestimation.

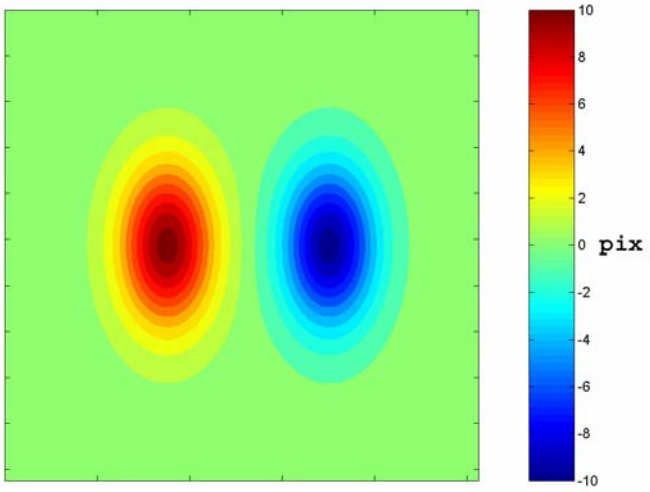

Fig. 3.5 Deformation on the *x*-direction applied to the simulated image to perform the simulation.

Number of imaged beads and background noise

The final resolution and accuracy of the computed displacement field depends on the number of imaged fluorescent beads. Since cross-correlation of image windows is used to compute gel displacement, windows containing no beads provide no information. Therefore, the concentration of imaged beads must be high enough to guarantee that most of the windows used at each iteration contain at least on bead. If this is not true, then the resulting values of an iteration are not corrective displacements, but only interpolated values of displacement. As a result of that iteration, the spatial resolution will be doubled but it will provide only a smoothed and interpolated field, without increase in accuracy. Therefore, to optimize our traction microscopy experiments, the number of imaged beads should be as high as possible. This number depends on the depth of focus of the microscope's objective and the concentration of beads used to construct the gel.

In our traction microscopy experiments fluorescent beads were found throughout the gel depth. Keeping in mind that we are only interested in the beads located at the top of the gel, all other imaged beads that are out of focus will result in background noise. Therefore, this noise will also depend on the depth of focus of the objective and the

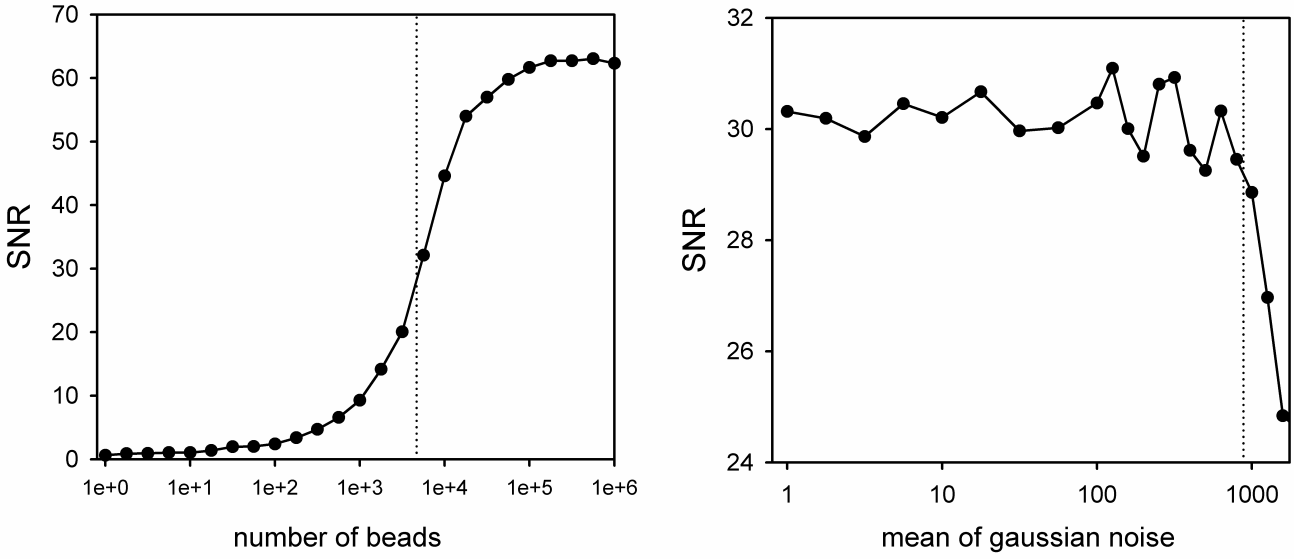

Fig. 3.6. Effect of bead number (left) and mean of gaussian noise (right) on the signal-to-noise ratio computed for the performed simulations. Peak displacement used for the simulations was 10 pixels. Vertical dotted lines correspond to the mean values of fluorescent beads per image (left) or background noise (right) obtained from real fluorescence images of the gels used for traction microscopy experiments.

number of imaged beads out of focus. Consequently, the background noise is also related to the number of imaged beads. The higher the concentration of beads used (and therefore the number of focused beads imaged), the higher the background noise observed.

An optimal bead concentration must be established in order to provide enough imaged beads but still keeping the background noise low. This relationship is shown in Fig. 3.6. It can be observed that the SNR increases as the number of imaged beads is increased. On the other hand, SNR decreases as the background noise tends towards the pixel intensity of the beads. The dotted lines indicate the values used in our traction microscopy experiments. Therefore, this results show that the concentration of beads used was conveniently adjusted to allow sufficient imaged beads while keeping background noise low enough.

Amplitude of the peak of displacement and effect of the max parameter

The cross-correlation algorithm allows computation of large displacement with high accuracy and spatial resolution. Nevertheless, too large displacements induce bead misidentification and result in erroneous displacements. Simulations were performed to establish the maximal amplitude of displacement that could be resolved by our software. The software to compute the displacement field allows setting up the max parameter in order to reduce noise in the resulting field. This parameter establishes the maximal corrective displacement permitted at each iteration (window size/max). Nevertheless, care should be taken to establish an optimal max value, since setting this parameter too high will result in underestimation of the real displacement. Simulations were performed for different peak amplitudes and max values to establish the optimal max value for each range of observed measurements. Fig. 3.8 shows SNR for different peak amplitudes and max values. It can be observed that using optimal amplitudes and max combinations, a good SNR is obtained for amplitudes ranging from 6 to 30 pixels (Fig. 3.7 left). Nevertheless, it should be noted that using too high max values will result in peak underestimation, thus decreasing SNR (Fig. 3.8). Fig. 3.7 right shows the optimal max value for each peak amplitude, and can thus be used to select the best max value for each experiment.

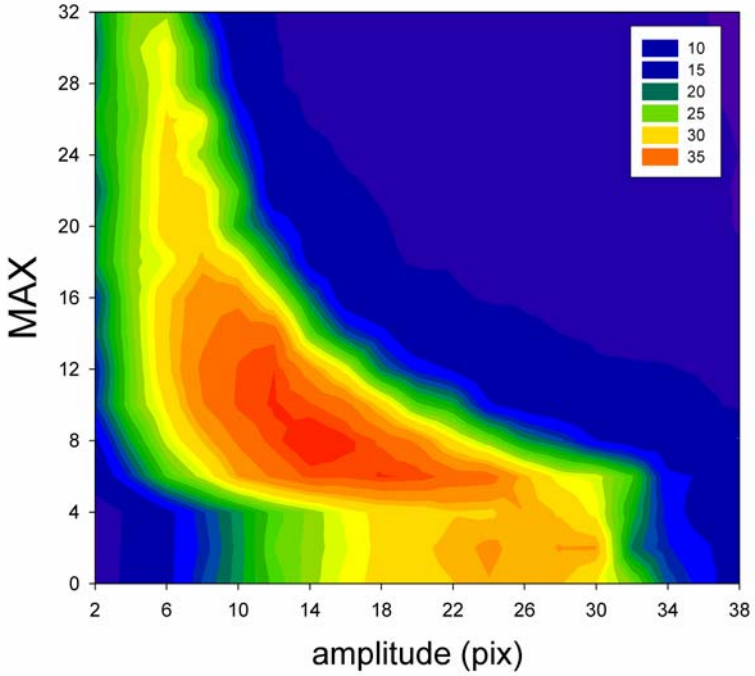

Fig. 3.8 SNR for different amplitudes and max values. Simulations were performed using simulated images as described in section (Generation of deformed bead images) above.

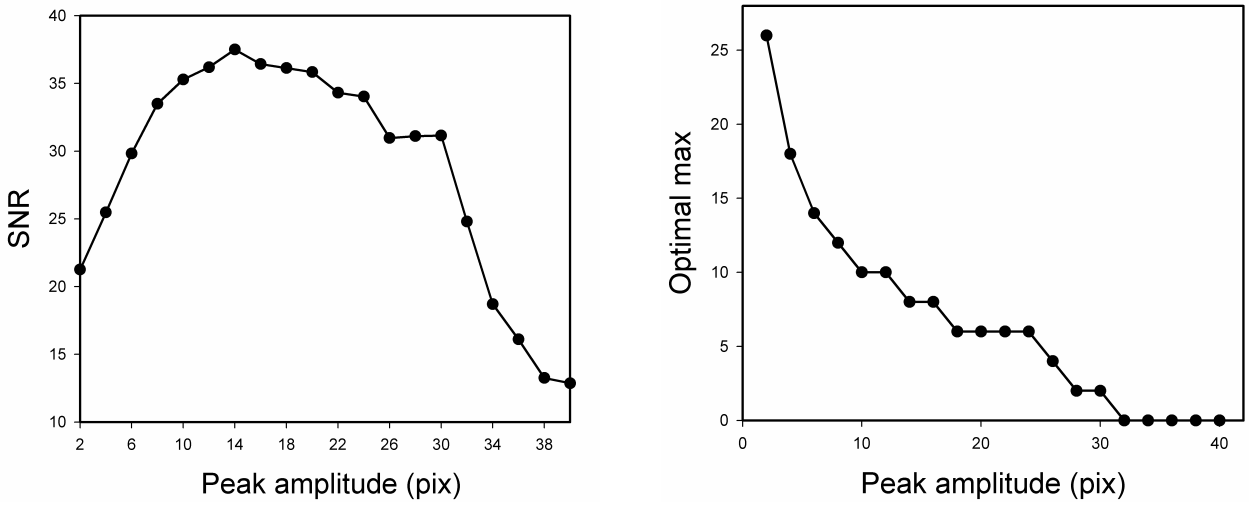

Fig. 3.7 For each peak amplitude in Fig. 3.8, the max value was adjusted to provide the highest SNR ratio. Left: Highest SNR obtained for each peak amplitudes. Right: Max value which provided the highest SNR for each peak amplitude.

3.4.2 Computation of the traction field

Effect of the selected cell contour

Constrained FTTC uses information of the cell contour to compute the resulting traction field from the previously computed displacement field. As a consequence, incorrect determination of the cell boundary may induce artefacts in the obtained traction field. Concretely, ambiguities often arise in determination of the cell boundary from a brigthfield image of the cell. For instance, well spread cells may have flat lamellipodia and thin protrusions whose tips are not clearly visible in bright field images. To address this question, we performed computer simulations in order to assess the effect of an incorrectly determined cell boundary on the resulting traction field.

The projected area of an imaginary cell was designed as a 17×35 pix rectangle, placed into the same 127×127 pix grid used in real traction microscopy experiments (Fig. 3.9 left). An artificial traction map was constructed within the projected area of the cell as shown in Fig. 3.9 mid. *X*–traction was chosen to be a linear function of the *x*–coordinate, whereas *y*–traction was set to zero. Next, the displacements were calculated using the forward problem from the Boussinesq solution. Poisson's ratio was set to 0.49, and the Young's modulus to 389 Pa. In addition, Gaussian noise (SD=0.25 μm) was added to the computed displacement field (Fig. 3.9 right). To test the effect of the cell boundary on the traction field recovered using CFTTC, different cell boundaries were constructed, ranging

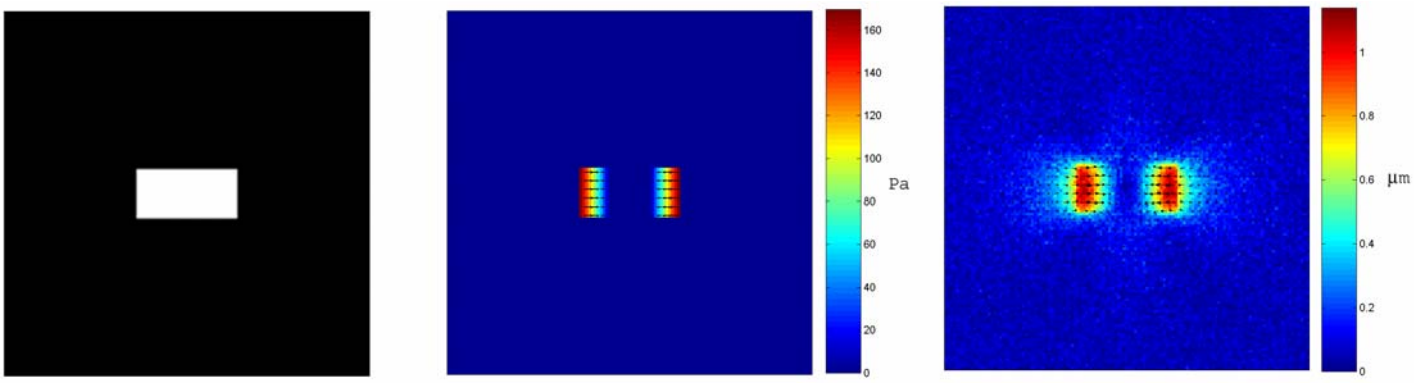

Fig. 3.9 Simulated cell area (left), simulated traction field (mid) and corresponding displacement field (right) computed using the forward approach to the Boussinesq solution. Gaussian noise (SD=0.25μ) was added to the displacement field.

from 5x23 pix to 53x71. The traction field was then recovered from the displacements using our standard CFTTC software. For each recovered traction field, the difference with the theoretical traction field was computed as $Diff = \sum_{x,y}\left(T_{theo}(x,y) - T_{comp}(x,y)\right)^2$. A number of 25 simulations were performed for each cell boundary.

Fig. 3.10 displays the difference (*Diff*) with respect to the theoretical field for cell contours of increasing border size. The figure shows that drawing the cell boundary too big did not introduce significant errors in the traction field, whereas using a cell boundary that was too small introduced serious errors in the traction field. Therefore, if the exact location of the cell boundary can not be clearly determined, it is better to define the cell boundary somewhat larger.

Effect of noise on the parameters reflecting cell contractility

To characterize the effect of noise in the displacement on the resulting total force magnitude, net contractile moment and strain energy, we performed simulations where the displacement field consisted of pure noise (Butler et al., 2002). We performed 200 simulations using the same cell contour (see Fig. 3.9, left) and gel characteristics as in the simulations described above. The displacement noise was Gaussian with standard deviation ranging from 0.05 to 0.5 μm. The traction field was computed using CFTTC.

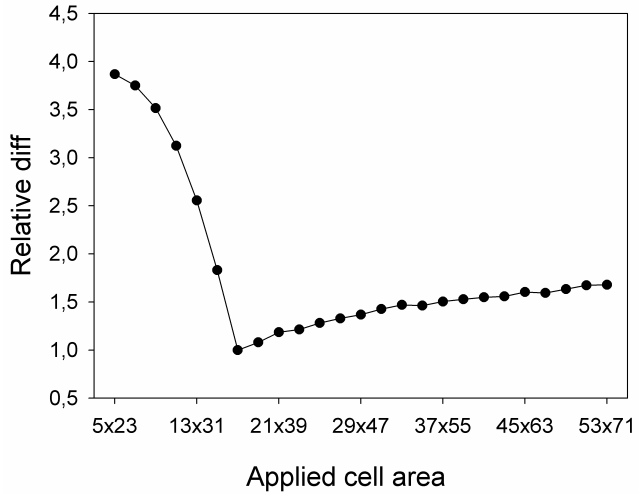

Fig. 3.10. Effect of applying an incorrect cell border for CFTTC computations. The difference (Diff) values are normalized to the Diff value obtained for the correct cell contour (17x35). See text for explanation on the computation of Diff.

The results of the simulations are depicted in Fig. 3.11. The effect of the noise on the net contractile moment was not significantly different from zero. This was expected, because the tractions are linear functions of the displacements and the expectation values of the noise in the displacements are zero. Nevertheless, it is important to know the expected magnitude of the departure from zero for each single simulation. The standard deviation of the net contractile moment increased linearly with the magnitude of introduced noise. The effect of noise on the total force magnitude was different from zero and increased linearly with increasing levels of noise. This was expected since total force magnitude uses the absolute value of the observed tractions. Therefore, although the expected values of the noise in the displacements and tractions are zero, the expected value of its absolute value is non-zero. The effect of noise on the strain energy was quite different; unlike the tractions and the moments, which are linear functions of displacement, the strain energy is quadratic. This implies that the expected value of the strain energy due to pure noise is also non-zero. Accordingly, in our simulations we found that the energy

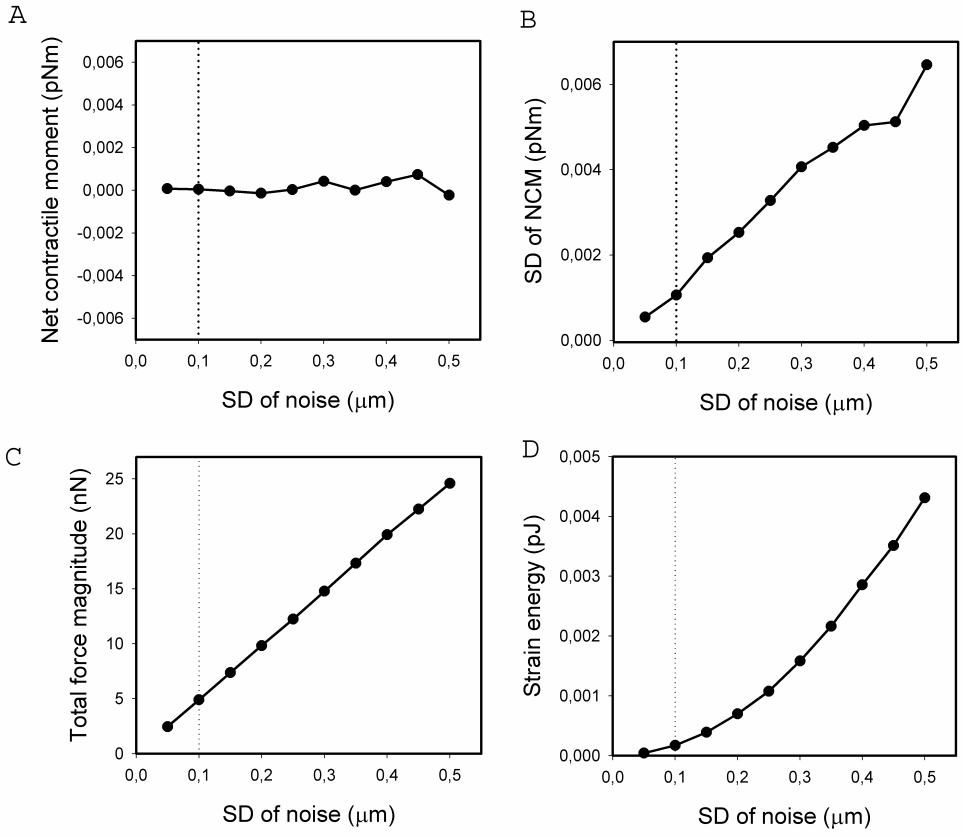

Fig. 3.11 Effect of noise in the parameters reflecting cell contractility. A. Net contractile moment. B. Standard deviation of the net contractile moment. C. Total force magnitude. D. Strain energy. Dotted lines correspond to the typical displacement noise obtained in real traction microscopy experiments.

associated with displacement noise increased quadratically with noise magnitude.

3.4.3 Determination of the cell contour

Unlike most of the previously published studies on TM, the contour of the cell was objectively assessed from a bright field image of the cell acquired at the beginning of the experiment. Accordingly, an algorithm based on the use of a Sobel filter was programmed to determine of the contour of the cell. The procedure, illustrated in Fig. 3.12, is as follows:

1. The image is filtered with a Sobel filter. The Sobel filter is a highpass filter and is thus used to highlight the zones of the image where the changes in pixel intensity are larger. In bright field and phase contrast images of adhered cells these zones correspond to cell borders.
2. The resulting image is binarized using a threshold value. As a result, pixels corresponding to the cell border and its proximity are set to 1 while the other pixels are set to 0. Nevertheless, some single pixels throughout the image are also set to 1.
3. The image is eroded to eliminate single pixels with values set to 1.
4. The image is dilated to recover the eroded pixels corresponding to the cell border.
5. All the particles in the binary image are listed, and only the one with the largest area is selected.

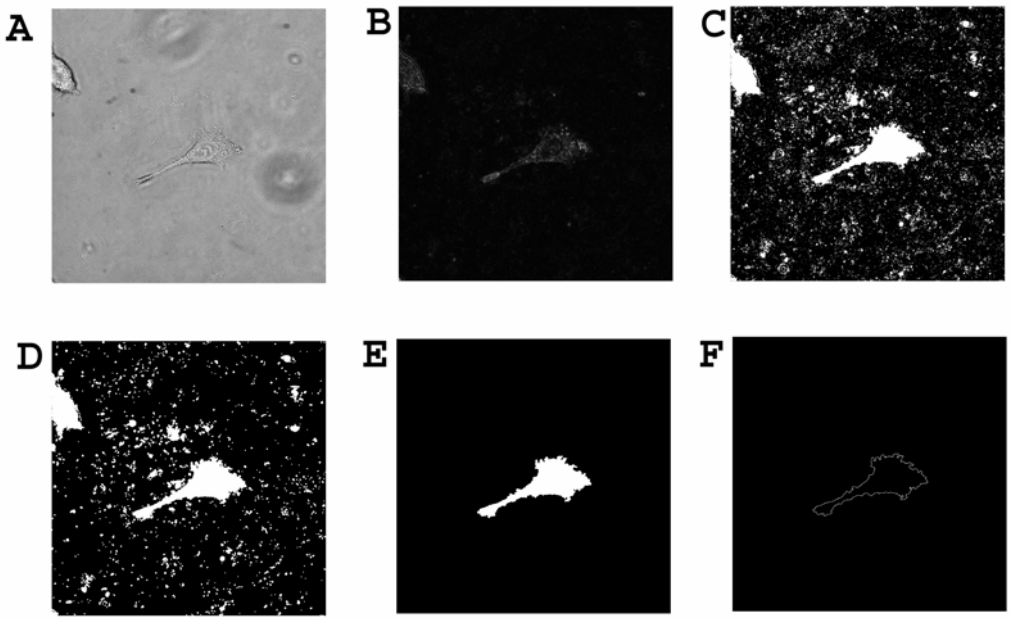

Fig. 3.12 – Determination of the cell contour. A. Bright field image of the cell. B. Image filtered with a Sobel filter. C. Thresholded image. D. Eroded and dilate image. E.Selection of the particle with the largest area. F. Contour of the selected particle.

6. The selected particle is filled to eliminate holes inside it, and its contour is subsequently computed. The filled particle and the computed contour are stored to be used as the cell area and cell contour.

The threshold value described in step 2 is the only parameter established for each cell image. By changing this parameter, the contour that best fits the cell can be selected, while detecting some more subtle parts such as filopodia.

The software written to perform this algorithm is displayed in Appendix D. The software was programmed using LabVIEW (National Instruments, Austin, TX).